J Mater Sci (2007) 42:7850–7860
DOI 10.1007/s10853-007-1620-z

Sensitivity of damage to microstructure evolution occurring during long-term high-temperature annealing in a semi-crystalline polymer

Sylvie Castagnet · David Girard

Received: 29 June 2006 / Accepted: 16 February 2007 / Published online: 1 June 2007

Abstract This study aimed to highlight the role of microstructure evolutions induced by high temperature annealing on damage in a semi-crystalline polymer during long-term applications. It was based on a polar form of poly(vinylidene fluoride) (T_g = –40 °C; T_m = 170 °C) and the long term annealing context dealt with burst resistance tests performed for 1000 h in a temperature range from 95 °C up to 140 °C. A secondary crystallization was observed after annealing by Differential Scanning Calorimetry and a consistent phenomenology was evidenced in Dynamic Mechanical Analysis. A decrease of the amorphous phase mobility and a weak reorganization of primary crystals were observed at the same time. Tensile tests on annealed specimens pointed out modulus and yield stress reinforcement, partial disentanglement in the amorphous phase and a raise of the volume strain. Thermally-induced microstructure evolutions were shown to enhance cavitation and slow down crack opening displacement kinetics. This last effect would result from both a raise of the yield stress in primary crystals and secondary crystallization.

S. Castagnet (✉) · D. Girard
Laboratoire de Mécanique et Physique des Matériaux (UMR CNRS 6617), ENSMA, 1 Avenue Clément Ader, BP 40109, 86961 Futuroscope cedex, France
e-mail: castagnet@lmpm.ensma.fr

D. Girard
Arkema, CERDATO, 27470 Serquigny, France

Introduction

The design of polymeric pieces of a engineering structure, which mainly involve semi-crystalline thermoplastics, requires an accurate prediction of lifetime and thus a good understanding of damage processes. It is all the most important for long-term applications like pressure pipes or vessels used at high temperature. The nucleation and growth of micro-voids, which further leads to crazing and crack propagation, is a well-known phenomenon in polyethylene (PE), polyoxymethylene (POM) or polypropylene (PP) [1–7]. Many works were published about cavitation micro-mechanisms in rubber-toughened polymer but the key problem mainly involves rubber particles and differs from our issue. When strained in particular strain-rate and temperature conditions, micro-voids considered here in semi-crystalline homopolymers were nucleated within amorphous layers. This cavitation process has been crucial in slow crack growth issue for instance: when tested in this regime (high temperature and low internal pressures) failure has been resulting from the propagation of a very thin and short crack across the pipe wall. The onset of cavitation and nucleation of a porous area was identified then as a slow crack growth precursor [8].

Cavitation is bound to depend on (i) the local morphology of crystalline lamellae inducing local hydrostatic stress within the amorphous layers, (ii) the local amorphous flow ability directly linked to strain-rate and temperature, (iii) the external stress field and the hydrostatic stress in particular. So, any thermo-mechanical treatment affecting the crystalline microstructure was expected to have consequences on damage processes. The following stage of crack propagation also depends on microstructure. Stiffness and structural disorder were pointed out as influent parameters in slow crack growth resistance in PE [9].

High temperature annealing is known to activate some microstructure changes in semi-crystalline polymers [10–16]. These works reported a critical temperature T_{c0}, close to the main melting temperature, above which annealing induces a thickening of lamellae. This process requires a great mobility of chains within lamellae. On the contrary, the thickness of primary lamellae remains unchanged during annealing below T_{c0}: a secondary crystallization is then observed corresponding to the formation of ordered volumes in the amorphous phase.

This study aimed to investigate how micro-structural reorganizations induced by a high temperature annealing—directly affecting the lamellae shape and the amorphous phase mobility—enhanced or not cavitation and crack propagation processes in such a material when strained. It is based on apolar form of poly(vinylidene fluoride) (alpha crystalline phase) (PVDF) in the framework of burst resistance tests performed at high temperature for several 1000 h.

The first part of the paper deals with the microstructure changes occuring during such long term annealing (several 1000 h) for temperatures higher than 95 °C. DSC and DMA experiments were performed. Via moduli, DMA spectra allowed to link elementary mechanisms to the mechanical behaviour pointed out in the second part of the paper. Tensile tests were performed with a particular attention paid on volume changes resulting from cavitation. Creep tests on notched specimens were also carried out to investigate consequences on cracking.

Experimental

Materials

The PVDF studied here was a commercial homopolymer (Kynar740®) by Arkema. All samples were machined in extruded pipes (external diameter 32 mm; thickness 2.5 mm) after different thermo-mechanical histories summarized in Table 1, i.e. machined in as-received pipes (AR) and in pipes failed after slow crack growth during burst tests performed at different temperatures (Table 1). Effects of annealing time, annealing temperature and weak pressure loading could not be separated from each other. Nevertheless, annealing time variations were about 10% from the mean value. After failure in the slow crack growth regime, the pipe was further unloaded and often kept at the test temperature before removing from the device. Creep deformation could not be measured during burst resistance test. Nevertheless, it must have been rather low since the pipe dimensions measured at the end of the experiment were nearly the same as initially. A few comparisons have been performed here on samples annealed at 120 °C for 1440 h without any mechanical loading to point out the possible effect of the low pressure applied to the pipes during burst tests described above.

Table 1 Thermo-mechanical history of the tested aged materials after burst resistance test

	Temperature during burst test (°C)	Lifetime (h) (SCG failure)	Hoop stress (Mpa)
V95	95°C	3595	11.5
V120	120°C	4381	8
V140	140°C	4043	4.8

All samples spent at least several weeks at room temperature between the end of burst resistance tests and DSC or DMA experiments.

Differential scanning calorimetry (DSC)

Experiments were performed under a N_2 sweep in a TA Instrument DSC-2920 used in a standard mode. Measurements were taken on samples of 10 mg at least and cut in the same pipes. The temperature range was from –70 °C up to 200 °C at heating and cooling rates equal to 5 K/min. Two scans were performed for each experiment. Measurements allowed an evaluation of the weight fraction extent of crystallinity χ as following:

$$\chi = \Delta H_f\ (T_m)\ /\Delta H_f^0\ (T_m^0) \quad (1)$$

where $\Delta H_f(T_m)$ is the enthalpy of melting measured by integrating the melting peak and $\Delta H_f^0(T_m^0)$ is the enthalpy of melting of the totally crystalline polymer at the equilibrium melting temperature. A value of 104.6 J/g was taken for ΔH_f^0 [17]. Measurement of the melting peak area was based on a linear extrapolation of the baseline from the melt. Calculations from a series of ten experiments performed on the same material and same operating conditions lead to a discrepancy of ±0.6% for χ. The crystallization temperature was 149 °C for all materials tested here. It was checked that the melting temperature (170.4 ± 0.2 °C), crystallinity ratio (53.5 ± 0.5%) and shape of the melting peak are identical for all tested specimens on the second scans after heating up to 200 °C.

Dynamic mechanical analysis (DMA)

These measurements were taken on a TA Instruments DMA-Q800 in a single cantilever mode. Samples were cooled down to –80 °C at 5 K/min with liquid nitrogen and kept at this temperature for 10 min before starting the linear temperature ramp from –80 °C up to 160 °C at a heating rate of 2 K/min.

Samples had a gauge length of 17.5 mm, a width of 5 mm and a thickness of about 2.5 mm. They were cut along the extrusion direction of the pipe and polished to make the upper and lower faces flat. Skins on the inner and outer surfaces were then removed. Because of the polishing treatment, thickness was not exactly the same for all samples and not perfectly constant all along each sample. Thickness discrepancy (±0.05 mm) resulted in a storage modulus discrepancy of ±6%. For temperatures higher than 150 °C, these thickness defects may have induced tightening problems but all samples were tight in the DMA device with a torque wrench up to the same clamping torque value of 0.132 Nm.

Experiments have been carried out at 1 Hz with a maximal amplitude of 15 μm corresponding to a maximal strain of 3×10^{-4}.

Tensile tests

Dumbbell specimens were machined in extruded pipes (external diameter 32 mm; thickness 2.5 mm) with half-scale ISO R527 specifications all in the hoop direction. Samples were machined in as-received (AR) pipes and in pipes previously submitted to the burst resistance tests depicted in Table 1. Uniaxial tensile tests were performed in an Instron Universal Test Instrument 1190. Specimens were tested at a constant strain-rate of 3×10^{-3} s^{-1} and constant temperature ranging from 100 up to 120 °C (±1 °C).

Up to necking, stress and strain could be considered homogeneous in any position on the gauge length. Logarithmic axial and transverse strain measurements were analysed and stored by the optical device consisting in four marks laid on the sample and followed by a digital image correlation software linked to a CCD camera. Hencky strains were calculated from Eq. (1):

$$\varepsilon_{\text{axial}} = \ln\left(\frac{l}{l_0}\right) \tag{1}$$

where l_0 and l are the initial and actual gauge length values.

Both the axial strain $\varepsilon_{\text{axial}}$ and the width strain $\varepsilon_{\text{width}}$ were measured with this device. Then, the volume strain ε_{vol} could be calculated according to Equation (2), assuming isotropy of transverse strains along width and thickness:

$$\varepsilon_{\text{vol}} = \varepsilon_{\text{axial}} + \varepsilon_{\text{width}} + \varepsilon_{\text{thickness}} = \varepsilon_{\text{axial}} + 2\ \varepsilon_{\text{width}} \tag{2}$$

Before necking, stress and strain were homogeneous in the sample. The local axial component of the Cauchy stress tensor $\underline{\underline{\sigma}}$ could be calculated then from Eq. (3):

$$\sigma_z = \frac{F}{S} \tag{3}$$

where F is the actual value of the axial force and S the actual value of the cross-section area calculated from the width strain $\varepsilon_{\text{width}}$ still assuming the isotropy of transverse strains.

Creep tests on notched specimens

A constant load was applied with a 1:10 lever creep device to a three-notched parallelepiped sample (length: 125 mm; width: 10 mm; thickness: 4.7 mm). The principal and lateral notches (1.5 and 0.5 mm deep respectively) were made with a razor blade (curvature radius 700 nm) penetrating slowly perpendicularly to the surface. To be sure that the principal notch and the lateral ones are in the same section, the latter ones were made under a binocular.

The applied stress was calculated in the notched section. The average initial value of the ligament area ($30\ mm^2 \pm 5\%$) was calculated from fourteen samples after a post-mortem measurement with an optical microscope. Two pairs of optical marks were drawn on the lips of the notch to measure the notch opening during the test. Photographs taken by the CCD camera were analysed with digital correlation software. Distances between the two marks of the same pair were measured and averaged to get the crack opening displacement (COD). Such a calculation assumed that the deformation of the notch lips could be neglected. All tests were performed at 120 ± 1 °C. Here, samples were submitted to low stresses corresponding to the slow crack growth regime in burst resistance tests. Electronic microscopy observations indicated that the process zone ahead of the crack tip was clearly delimited: the whole ligament was not plastically deformed.

Results and discussion

Microstructure modification after long-term annealing at high temperature

DSC thermograms of samples machined in pipes previously submitted to burst tests at different pressures and temperatures (95 °C, 120 °C and 140 °C) are presented in Fig. 1. The corresponding characteristics of thermograms are summarized in Table 2. DMA experiments have been performed to complete the understanding of thermally induced microstructure changes and to make a link with the mechanical consequences studied below. Figure 2 compares DMA spectra from an as-received sample to those machined in pipes after burst resistance tests at different temperatures. Several phenomena could be observed mixing these two techniques.

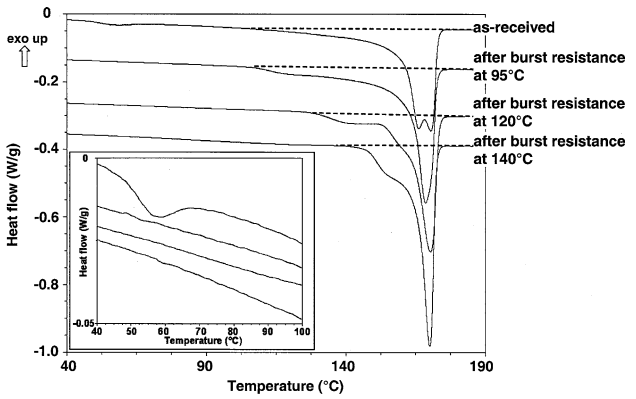

Fig. 1 DSC thermograms of as-received and thermally aged samples presented in Table 1 (first heating scan; 5 K/min)

Table 2 Characteristics of the DSC thermograms presented in Fig. 1

	Sample	Melting Temperature (°C)	Crystallinity Ratio (DSC)	Height of the main melting peak (W/g)	Width at mid-height of he melting peak (K)
As-received	AR	166.5/171	50.8%	/	/
Aged	V95	169	53.3%	0.391	6.7
	V120	170	55.4%	0.426	6.3
	V140	170	55.5%	0.591	4.3

Lower glassy transition

The peak centred at around –35 °C on tan δ in DMA spectra (Fig. 2) depicted the glassy transition. A 40% decrease of the storage modulus was classically observed at the same time. As often, the glassy transition was not clear on DSC thermograms.

Upper glassy transition

A small peak on tan δ with a maximum at 23 °C appeared after annealing in Fig. 2. This peak was not observed for the as-received material. The peak on tan δ or on the loss modulus became clearer for higher annealing temperatures. El Mohajir and Heymans [15] observed a similar phenomenon in PVDF after annealing 1 h at 150 °C and further annealing at temperature lower than 80 °C. It was associated with the upper glassy transition. Like for the lower one, no signature was observed in DSC thermograms.

Physical ageing at room temperature

For the as-received material, a small endothermic peak can be observed around 60–70 °C on the DSC thermograms in Fig. 1. It disappears on the second scan. For samples cut in the pipes previously submitted to burst resistance tests at a high temperature T_a and further raised to the temperature T_a just before the DSC experiments, no small endothermic peak was observed either around 60–70 °C. This endothermic peak corresponded to the melting of secondary

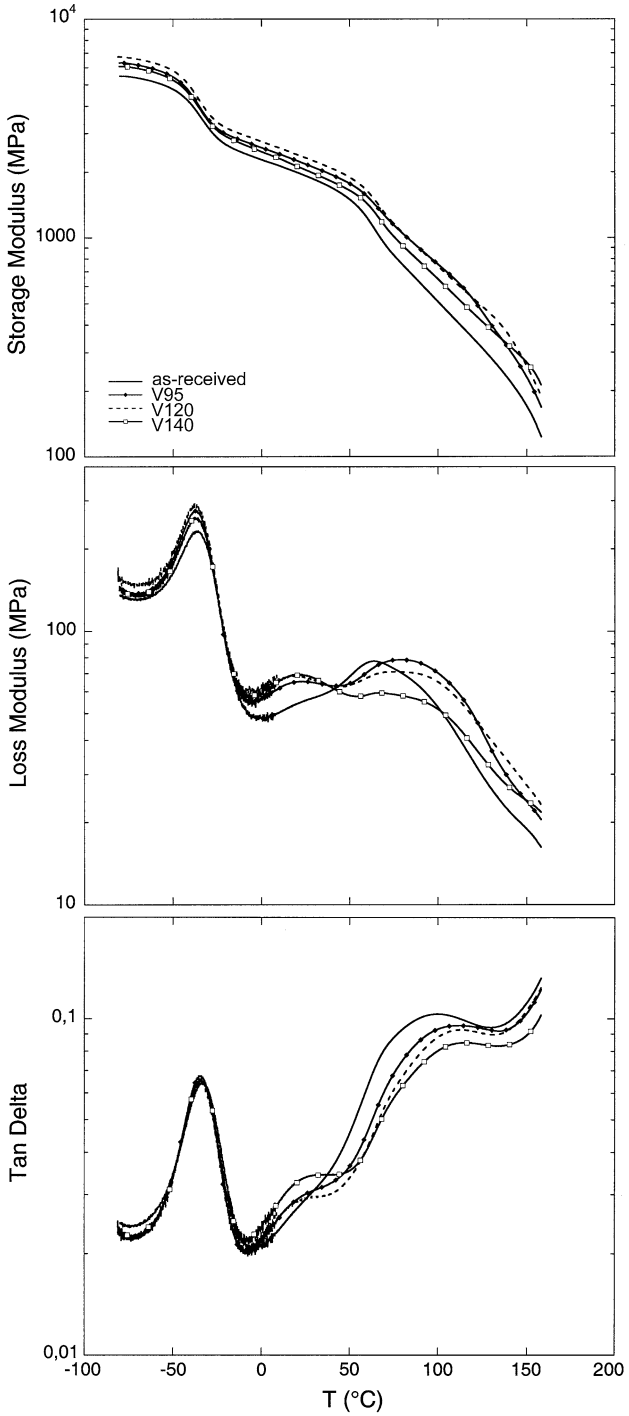

Fig. 2 DMA spectra obtained after burst resistance tests at different temperatures (see Table 1) (2 K/min)

crystals formed during the long time spent at room temperature before the DSC experiment [14]. The location of the peak changed with the time spent at room temperature between the annealing treatment and the DSC experiment.

After annealing at high temperature, samples aged during burst tests at 95 °C, 120 °C or 140 °C have been stored at room temperature for a long time before DMA experiments also. A drop of storage modulus appears around 70 °C on DMA spectra in Fig. 2, i.e. at the same temperature as the DSC peak. The corresponding peak on tan δ remains quite difficult to analyse since it appears like a shoulder of the α_c crystalline transition peak studied in the next section. The tan δ peak is better defined on spectra corresponding to annealed sample when the alpha transition peak is shifted towards the higher temperatures. On the second heating scan (performed on the V140 sample) both the shoulder on tan δ peak and the drop on storage modulus, visible on the first run have disappeared. Again, these phenomena could be regarded as a consequence of annealing at room temperature.

The presence of small crystalline arrangements enhanced by room temperature storage reduced the molecular mobility in the amorphous phase. This is in accordance with the RMN study performed by Neidhöfer et al. [14] pointing out a reduced mobility in the amorphous phase after annealing.

Secondary crystallization during annealing at high temperature

After high temperature annealing (typically above 120 °C) an endothermic peak appeared like a shoulder of the main melting peak on the first heating scan of DSC thermograms (Fig. 1). They were centred at around 120 °C, 140 °C and 155 °C after annealing at 95 °C, 120 °C and 140 °C respectively. Like those involved in room temperature annealing, these peaks disappeared on the second heating scan.

As already reported [10, 11, 14], it clearly evidenced a secondary crystallization process: small-organized volumes created at a given annealing temperature further melted at higher temperature. According to Marand et al [10, 11] small crystals nucleated at so high temperature constituted a specific population within the amorphous phase. Evidence was brought in ethylene/octene copolymers and PEEK of a critical temperature T_{c0} above which annealing induces a thickening of primary lamellae and below which the thickness of primary lamellae remained unchanged. An actual secondary crystallization was then observed, corresponding to the formation of ordered volumes within the amorphous phase. This interpretation was further developed by Neidhöfer et al. [14] for alpha-PVDF. In this polymer the secondary crystallization clearly appears for temperatures as low as room temperature and is very rapid for annealing at 140°C. As the main melting temperature remained nearly constant (170 °C), the average thickness of primary crystallites was considered as nearly unchanged after annealing.

The DMA signature of the melting of these secondary crystals looked like the one observed for annealing at room temperature. A fall of the storage modulus can be observed in Fig. 2 from 115 °C, 135 °C and 150 °C for samples aged at 95 °C, 120 °C and 140 °C respectively; a very quick raise of tan δ occurs in the same temperature range. The drop of storage modulus started at temperatures identical to endothermic peaks observed by DSC, i.e. at a higher temperature $T_d = T_a + \Delta T$ than the annealing temperature T_a. Like in our DSC experiments and already reported by Neidhöfer et al. [14] about DSC also, ΔT decreased when the annealing temperature is raised in DMA experiments. It led to a false peak in tan δ, difficult to analyse since it was included in the α_c massif analysed below. This earlier decrease of the storage modulus in DMA was fully consistent with the evolution of the main melting peak in the DSC experiments. The drop of modulus and the false tan δ peak could be attributed to the beginning of secondary crystals melting.

Primary crystals population

For the as-received material, the main melting peak in DSC thermogram (Fig. 1) exhibited a particular shape with two distinct peaks. It could be attributed to a difference of crystal size between the skin and the core of the pipe. It turned into a single melting peak located at 169 °C after 3595 h at 95 °C. Its particular asymmetrical shape could be linked to a size homogenization of the two lamellae populations: the low temperature melting peak (initially located at 166.5 °C) seemed to increase in temperature and become higher than the peak initially located at 171 °C. For samples aged at 120 °C and 140 °C, only the higher temperature-melting peak could be distinguished. The main melting peak became narrower and deeper for increasing annealing temperatures as indicated in Table 2. This could be due principally to a more homogeneous lamellae crystallites population and also to a decrease of defects density within crystallites. Homogenization of the crystallites size was allowed by the melting of smallest crystals during annealing. Indeed, the baseline extrapolated from the melt intercepted the experimental curve of the as-received material at $T_i = 108$ °C against 120 °C and 138 °C after burst resistance tests at 120 °C and 140 °C respectively. This means that, after a long term annealing at a given high temperature T_a, all crystals further melted at higher temperatures than T_a during DSC experiments.

After annealing, the crystallinity ratio significantly increased. Nevertheless, it was calculated from a linear baseline extrapolation from the melt including the shoulder appearing after annealing. The crystallinity ratio thus resulted as a global quantity mixing primary and small secondary crystals. From the contribution of the secondary crystallites melting enthalpy to the total melting enthalpy Neidhöfer et al. [14] evaluated the corresponding crystallinity ratio contribution to a few percent. This value corresponded to the apparent increase of crystallinity measured here after annealing. This meant that the apparent increase of crystallinity measured after annealing could be mainly attributed to the secondary crystals.

Figure 3 gives a comparison between the second heating scan on the as-received material and the first heating scan on a material previously submitted to a burst resistance test at 140 °C (V140). Melting temperatures were both equal to 170 °C but the crystallinity ratio during the second heating scan was lower (51.2%) than that obtained on the V140 sample. It could be concluded that a long term annealing at 140 °C during several 1000 h was more efficient for crystalline organization than a slow cooling down at 5 K/min.

DMA spectra in Fig. 2 show a broad peak, with a maximum around 100–110 °C. This peak, usually named ''α_c transition'', was attributed to the shear of amorphous layers allowed by the elongation of the tie molecules. This elongation was due to the translation of chains within the crystalline lamellae resulting from the activation of defects mobility in crystals according to a ''flip-flop'' mechanism [18, 19]. A consequence of molecular mobility within lamellae was to improve primary crystals rejecting some defects in the interphase. These defects were rejected in the

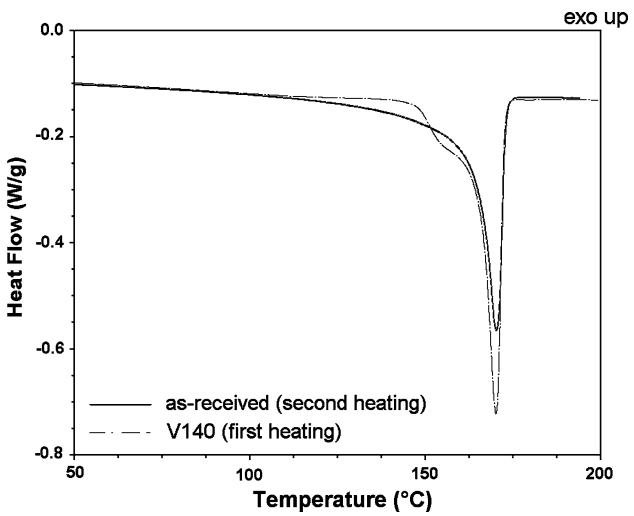

Fig. 3 Comparison between the second heating on the as-received material and the first heating on a material previously submitted to a burst resistance test at 140 °C (5 K/min)

vicinity of the surface of crystallites; they constituted an intermediate phase between crystalline and amorphous layers. This phase, closely linked to crystallites and less mobile than the amorphous layer, exhibited a glassy transition at the upper temperature T_g^{up} previously depicted. After annealing, chains mobility within crystallites was then reduced: as visible in Fig. 2, the maximal value of the peak on tan δ was shifted towards higher temperatures after high-temperature annealing during burst resistance tests i.e. from 99.2 °C for the as-received material up to 111.7 °C, 112 °C and 115.8 °C after burst resistance tests at 95 °C, 120 °C and 140 °C respectively. The height of the peak also decreased. Because of this shift towards higher temperature the storage modulus increased in the annealing temperature range. This evolution was due to more difficult motions in the amorphous phase and could be attributed to both the reduction of mobility of tie molecules and the nucleation of small secondary crystals within the amorphous phase. Quantitative analysis and interpretation of the α_c peak on tan δ was not easy because of the shoulder around 70 °C more or less clear depending on the thermo-mechanical history of the material.

Role of the low internal pressure applied during burst resistance test

Samples cut in pipes previously submitted to burst resistance test for a very long time have both undergone a thermal treatment and a low-pressure loading. During the test, deformation remained limited since each pipe recovered its original size after unloading. DSC experiments carried out after burst resistance test at 120 °C (V120) and after annealing at 120 °C for 1440 h without any mechanical loading (R120) provided similar results. In the latter case, the crystallinity ratio was 54.2% against 55.4% for the V120 sample. The melting temperature was slightly minor (168.5 °C) than the V120 sample (170 °C). The height of the main melting peak was nearly identical and the width at mid-height 1 K wider in R120 than in V120. The shoulder associated with secondary crystallization was located at a lower temperature for R120 (135 °C) than for V120 (140.5 °C) but the shorter annealing time for R120 would have explained such difference [14]. Thus, the small pressure applied during burst resistance tests at high temperature was regarded of minor importance in comparison to the role of thermal treatment.

Synthesis

An attempt to schematize consequences of high temperature annealing on both primary crystals and amorphous layers is proposed in Fig. 4:

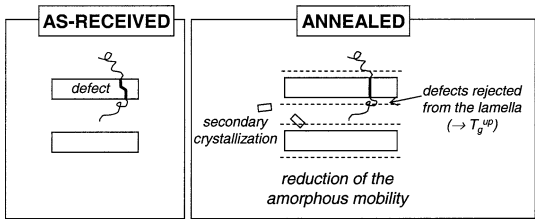

Fig. 4 Schematization of the consequences of high-temperature annealing during burst resistance test on the microstructure of alpha-PVDF at the lamellar scale

(i) The primary crystals population undergoes reorganizations among which a thickness homogenization, a probable enlargement and a rejection of defects out of crystalline lamellae. The latter process leads to a more defective constrained amorphous layer at the boundary of primary crystallites.
(ii) Annealing induces a secondary crystallization process within the amorphous phase.
(iii) As supported by our DMA experiments, the amorphous phase mobility decreased after high temperature annealing, consistently with anterior results by solid RMN concluding to conformational constraints induced in the residual amorphous by the formation of secondary crystals [14].

Comparisons between samples cut in pipes previously submitted to burst resistance tests and samples annealed at the same temperature without mechanical loading suggest that thermal annealing is the first order parameter in the microstructure changes observed here.

Mechanical behaviour

Such microstructure modifications were likely to affect the mechanical behaviour of materials when stretched at a lower temperature than the previous annealing temperature T_a. Classical tensile behaviour has been considered first. Next, a particular attention has been paid on damage initiation and crack propagation in the low stress range involved in the slow crack growth regime.

Modulus and yield stress

Evolution of the conventional stress with the conventional strain is depicted in Fig. 5 for a tensile test performed at 3×10^{-3} s^{-1} and 120 °C on the as-received material. The first stage referred to a homogeneous deformation of the specimen up to necking. During stage 2, the deformation was not homogeneous any more since the neck propagated along the gauge length of the sample. It corresponded to a spherulitic-to-fibrillar transformation of the material. After entire propagation of the neck, the material was further

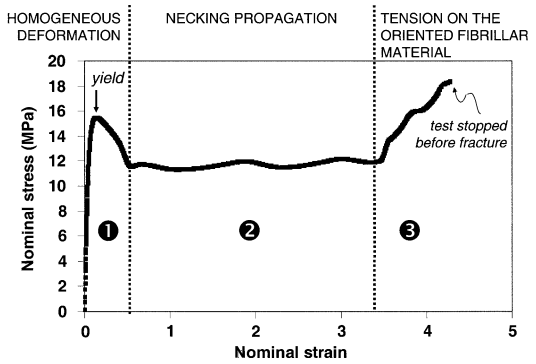

Fig. 5 Tensile test performed at 3×10^{-3} s^{-1} and 120 °C on the as-received material

stretched homogeneously again (stage 3). The oriented fibrillar microstructure showed a reinforced modulus.

Figure 6 compares the tensile behavior (stage 1) of as-received samples to that of specimens machined in pipes after burst resistance tests at 95, 120 and 140 °C. Tests were performed at 3×10^{-3} s^{-1} and 120 °C. Corresponding values of the modulus and yield stress are summarized in Table 3. The yield point was defined as the maximal strength point on the conventional stress-strain curve. Each value was averaged from three tests.

A raise of the modulus (from 14% up to 27% with increasing annealing temperature) was observed after annealing, consistently with the increase of storage modulus observed in DMA experiments. The yield stress also increased with the annealing temperature, from 17% after annealing at 95 °C up to 21% after annealing at 140 °C. All microstructure modifications may have contributed to this increase:

(i) Deformation was more difficult in a material containing more crystals and less mobile amorphous chains
(ii) Shear yielding of less defective lamellae needed a higher stress

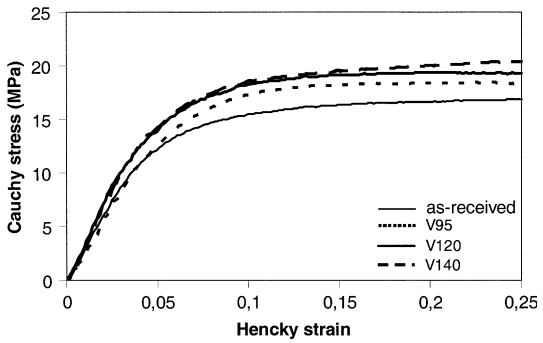

Fig. 6 Tensile behavior of as-received and annealed samples (3×10^{-3} s^{-1}; 120 °C)

Table 3 Modulus and yield stress measured for tensile tests presented in Fig. 6 (3×10^{-3} s^{-1}; 120 °C)

	As-received	V95	V120	V140
Yield Cauchy stress (MPa)	280	320	330	355
	15.7	18.4	18.9	19

(iii) Secondary crystallization decreased the global amorphous mobility and contributed to a toughening of the material. The role of secondary crystals has been emphasized by tests performed at 120 °C on samples previously annealed at 95 °C. In this case, secondary crystals previously formed during annealing at 95 °C have melt, as observed in DSC and DMA experiments. Modulus and yield stress measured at 120 °C after annealing at 95 °C appeared lower than after annealing at 120 °C or 140 °C.

Both modulus and yield stress determined for the R120 sample annealed for 1440 h at 120 °C without mechanical loading (320 MPa and 18.7 MPa respectively) were nearly the same as for the V120 sample (330 MPa and 18.9 MPa respectively). Again, the weak pressure applied during burst resistance tests seemed to be of minor importance against annealing.

Natural draw ratio

During stage 2 (cf. Fig. 5), necking propagated all along the gauge length. Extension reached at the end of propagation defined the natural draw ratio λ_n. This parameter corresponded to the conversion from a spherulitic to a fibrillar microstructure. It was characteristic of the material microstructure. In a purely amorphous polymer, the natural draw ratio λ_n is directly linked to the entanglement density v_e according to the following relationship:

$$\lambda_n \propto \frac{1}{\sqrt{v_e}} \tag{4}$$

The higher the natural draw ratio λ_n, the less entanglements in the amorphous polymer. In the crystalline polymer at stake, the natural draw ratio was assumed to directly result from the amorphous phase behavior. Equation (4) was then used to calculate a density of entanglements in the amorphous phase. Table 4 presents λ_n values (average values calculated from 3 tests with a standard deviation of 0.05) measured in tension at 3×10^{-3} s^{-1} and 120 °C. Its relative evolution after annealing was compared to the as-received material in the last column. The natural draw ratio λ_n increased after annealing; the entanglement density consistently decreased. After burst resistance test at 95, 120 or 140 °C the entanglement density might have decreased from at least 13%, i.e. more than the experimental scatter. This very partial and local disentanglement seemed consistent with microstructure reorganizations like homogeneization, enlargement and slight thickening of primary crystals and notably with secondary crystallization occurring during annealing. It must be reminded that such reorganisations were allowed by the possible motion of defects within crystals occurring in the temperature range of the α_c crystalline transition.

Table 4 Sensitivity of the natural draw ratio measured in tension (3×10^{-3} s^{-1}; 120 °C) to annealing and comparison of corresponding entanglement density compared to the as-received material

	λ_n	$\frac{v_c}{v_c(\text{as-received})}$
As-received	4.13	1
V95	4.57	0.8
V120	4.47	0.85
V140	4.43	0.87

The natural draw ratio measured on the sample annealed for 1440 h at 120 °C without loading (R120) was 0.9 times that of the as-received material. A partial disentanglement was observed but less important than in the V120 sample.

Volume changes and cavitation

Consequences of a long-term high-temperature annealing on cavitation were examined. A previous work established that cavitation in PVDF was very sensitive to temperature [20]. In as-received specimens strained at 3×10^{-3} s^{-1}, whitening and SAXS diffusion vanished for temperatures increasing from the ambient up to 150 °C and disappeared above a critical temperature T_c = 90 °C. Cavities nucleation also depended on strain-rate [20]: T_c increased with the strain-rate.

Dumbbell samples compared in Fig. 7 were machined in an as-received pipe and in a pipe previously submitted to a burst test resistance at 120 °C (V120). Volume strain was measured during tensile tests performed at a temperature (100 °C) and strain-rate (3×10^{-3} s^{-1}) close to critical values mentionned above.

The volume strain measured in the annealed specimen after 4380 h spent at 120 °C during the previous burst test was significantly higher than the one for the as-received material. At the beginning, values were identical in the as-received and aged specimens. It corresponded to the elastic contribution due to a Poisson ratio minor than 0.5. From an axial strain of 3%, the volume strain measured in the aged sample exceeded that of the as-received sample. The difference was greater than the experimental scatter. With this experimental device, volume strains measured in the

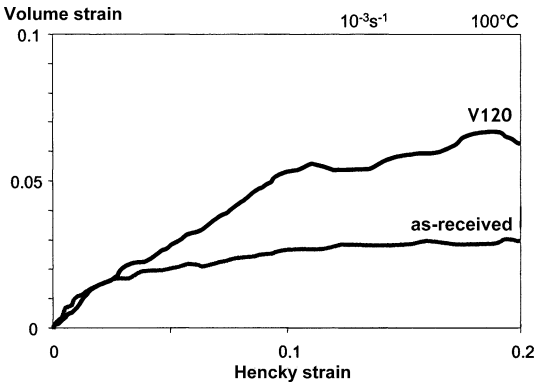

Fig. 7 Volume change measured in as-received and annealed (after burst resistance test at 120 °C) specimen stretched at 100 °C and 3×10^{-3} s^{-1}

sample previously annealed at 120 °C for 1440 h without mechanical loading (R120) was nearly the same as in the V120 sample.

Tensile tests have been performed at 100, 105 and 110 °C to estimate the critical temperature T_c above which whitening vanishes. As already mentionned, the as-received material remained translucent above 100 °C while the aged material (V120) exhibited a strong whitening at 100 °C, decreasing at 105 °C and vanishing at 110 °C. The critical temperature at which cavitation disappeared was higher in the sample previously submitted to a long lasting burst test at 120 °C.

Both the local and the macroscopic hydrostatic stresses were likely to influence cavitation.

(i) The local hydrostatic stress was influenced by the crystalline microstructure. Even if scales and materials are not the same as considered here, a comparison could be dared between the local strain into interlamellar amorphous phase between two lamellae and the well-known schema from Gent et al. [21] on strain cavitation in a rubber layer between two plates pulled apart from each other: the larger the plates, the higher the local hydrostatic stress at the middle point of the amorphous layer between them. Accommodation of the local deformation required large displacement of macromolecules in the amorphous phase. Modifications of the crystalline microstructure and amorphous mobility by annealing were thus likely to affect cavitation through the local heterogeneous stress-field within interlamellar amorphous layers and the hydrostatic stress in particular. The reduction of amorphous phase mobility, a slight enlargement and thickening of crystalline lamellae that raised the local hydrostatic stress at the middle point and a small decrease of the entanglement ratio were factors expected to enhance cavitation, as observed in tensile tests. Further growth of cavities implied large deformation of the material around them. It involved disentanglement in the amorphous phase and plasticity of crystalline lamellae. All these phenomena resulted in a larger volume strain observed in dumbbell specimens after annealing at high-temperature, for instance here during burst resistance tests.

(ii) The macroscopic hydrostatic stress deals with the geometry of piece. In our dumbbell specimens, the triaxiality ratio τ (defined as the hydrostatic stress over the equivalent Von Mises stress) calculated in an elastic framework was equal to 0.33, whatever the point in the gauge length. Conversely, a gradient of τ seated in the pipe wall. At any point M in the wall of a thin elastic pipe, τ was given by Eq. (5) (details for calculations are given in the Appendix):

$$\tau = \frac{\sigma_h}{\sigma_{VM}} = \frac{1}{\sqrt{3}} \frac{r^2}{R_e^2} \tag{5}$$

where r is the distance of the considered point M to the axis of the pipe and R_e is the internal radius of the pipe. The porous zone appearing in the pipe wall at the beginning of the slow crack growth process was located just below the inner skin [8]. Then, the triaxiality ratio was equal to 0.41. It was not so different from that calculated in the dumbbell specimen. Nevertheless, at temperature high enough (above 110 °C) no volume strain was measured in the latter whereas cavities ended up nucleating within the pipe wall (first stage of damage before initiation of the crack) [8]. Conclusions of this study suggested that microstructure changes induced by a long lasting application at high temperature would contribute to damage nucleation. It must be underlined that the triaxiality level of samples considered here (dumbbell or pipes) remained quite low. The relative influence of microstructure changes during annealing is bound to decrease for higher triaxiality ratio in the specimen.

Crack propagation

Microstructure changes were also expected to influence further stages of damage once the porous zone nucleated within the pipe wall has turned into an actual crack. Consequences of long-term high temperature annealing on cracking were investigated through creep tests on notched specimens. Samples were submitted to a constant load; the corresponding stress level σ in the ligament belonged to the hoop stress range involved in slow crack growth phenomenon during burst resistance tests. After loading, the crack opening displacement (COD) rate $\dot{\delta}$ slowed down to a stationary rate actually measured for 5 days in these tests.

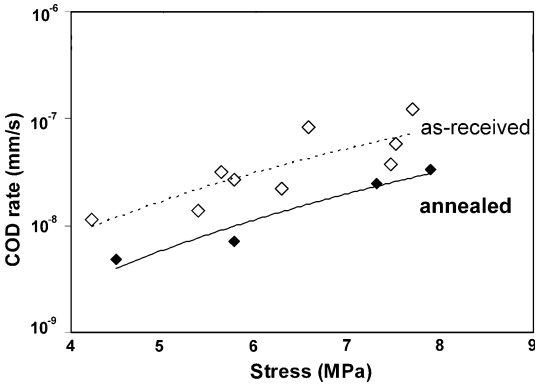

Fig. 8 Influence of annealing on the stress sensitivity of the crack opening displacement rate measured during creep tests on notched specimens at 120 °C

These COD rates are drawn vs. the applied stress in the ligament in Fig. 8, for the as-received material and after annealing for 5 months at 120 °C. In both cases, the COD rate depended on the applied stress in the ligament obeying a power-law:

$$\dot{\delta} \propto \sigma^n \tag{5}$$

where n is a stress-sensitivity parameter.

For a given applied stress level, the notch opening was slower in annealed samples than in as-received ones. Nevertheless, the stress-sensitivity parameters n were close, respectively equal to 3.55 for the as-received material and 3.61 for the annealed one.

This decrease of the COD rate after annealing could result from a raise of the yield stress σ_y in the process zone ahead of the crack tip. Figure 9 compares the COD kinetics in as-received and annealed samples submitted to creep stress corresponding to the same σ/σ_y ratio. Even in this case, the COD rate was slower in the annealed sample

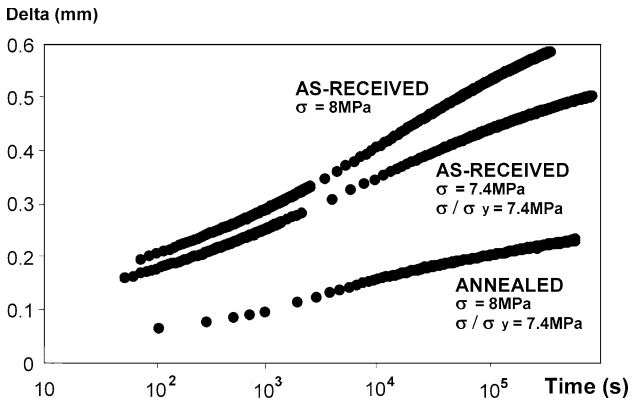

Fig. 9 Crack opening displacement kinetics measured during creep tests on notched as-received and annealed specimens at 120 °C: effect of the stress/yield stress ratio

suggesting that kinetics differences could not be attributed to a yield stress effect only.

Indeed, crystals plasticity, disentanglement and secondary crystallization were found to influence the mechanical resistance of the fibrillar process zone of the crack and consequently the crack opening and propagation. Nevertheless, it remained rather difficult to separate each contribution. Disentanglement would have resulted in an earlier fracture of fibrils within the process zone and lead to a higher crack opening. Nevertheless, for the same applied stress, the raise of the yield stress would have delayed plasticity in the process zone and contributed to a lower COD. Secondary crystals would have a major effect then, acting as supplementary ''cross-links'' in the macromolecular network and decreasing the amorphous phase mobility.

Conclusion

This study aimed to highlight the contribution of microstructure changes induced by high temperature annealing to damage processes. Consequences of annealing have been studied first with a focus on long durations (several 1000 h) at high temperatures (90–140 °C). Results from DSC experiments supported an evolution of the amorphous phase consistent with those previously observed on alpha-PVDF annealed for shorter times or at lower temperatures. Annealing above 95 °C induced an improvement of the structure and a size homogenization of the primary crystals population which led to a thinner main melting peak on DSC experiments. Secondary crystals have been nucleated at a given annealing temperature. They melted at a temperature higher than the annealing temperature. Whatever on DSC or DMA experiments, consequences of annealing at T_a (endothermic peak on DSC thermograms; tan δ peak and drop of the storage modulus on DMA spectra) were observed at a higher temperature $T_c = T_a + \Delta T$. ΔT decreased when the annealing temperature was raised. The correlated reduction of the amorphous phase mobility was responsible for a shift of the α_c crystalline transition peak on tan δ in DMA experiments. The mechanical loading applied during burst resistance test appeared of minor importance on microstructure evolutions since samples annealed at the same temperature without any mechanical loading exhibited similar evolutions.

Crystalline reorganizations, secondary crystallization and decrease of the amorphous phase mobility modified the local triaxiality ratio in the amorphous layers. In a low triaxiality context as involved in a dumbbell specimen a higher cavitation resulted from annealing above 95 °C. Partial disentanglement occuring during crystalline reorganizations and pointed out through a decrease of the

natural draw ratio was expected to assist cavities growth. As macroscopic triaxiality ratio in the thin pipes considered here was close to the dumbbell specimen value, a non negligible contribution of thermally-induced microstructure changes to cavitation onset in high-temperature application like burst resistance tests could be established. Microstructure evolution occuring during long-term annealing at high temperature also influenced the further damage stage of cracking. Partial disentanglement was likely to decrease the ultimate behaviour of fibrils and consequently enhance crack opening and propagation. Nevertheless, crack opening displacement kinetics was lower in annealed samples. It could be explained by a reduced plasticity enhancement in the process zone (due to the raise of yield stress in primary crystals), and by secondary crystals which acted as supplementary ''cross-links'' in the macromolecular network.

Acknowledgements Dr. J.L. Gacougnolle must be greatly acknowledged for his constant interest in this study and very precious remarks, as well as Pr. A. Dragon for his help in finalizing this paper. Authors would like to thank Arkema for financial support and PhD grant to D. Girard, and thank Dr. G. Hoschstetter for fruitful discussion.

Appendix

The following equations are valid for a thin elastic pipe subjected to a constant internal pressure P. The internal and external radii of the pipe will be called a and b respectively. Consider any point M of the pipe wall located at a distance r from the axis of the pipe.

The components of the stress tensor for M are the followings:

- radial stress : $\sigma_r = P\frac{a^2}{b^2-a^2}\left(1-\frac{b^2}{r^2}\right)$
- tangential stress : $\sigma_t = P\frac{a^2}{b^2-a^2}\left(1+\frac{b^2}{r^2}\right)$
- longitudinal stress : $\sigma_l = P\frac{a^2}{b^2-a^2}$

The hydrostatic stress is then $\sigma_H = \frac{1}{3}(\sigma_r + \sigma_t + \sigma_l) = P\frac{a^2}{b^2-a^2}$.

The Von Mises equivalent stress is:

$$\sigma_{VM} = \sqrt{\frac{1}{2}\left[(\sigma_r-\sigma_t)^2+(\sigma_r-\sigma_l)^2+(\sigma_t-\sigma_l)^2\right]} = \sqrt{3}P\frac{a^2b^2}{(b^2-a^2)r^2}$$

Then, the triaxiality ratio is given by:

$$\tau = \frac{\sigma_H}{\sigma_{VM}} = \frac{r^2}{\sqrt{3}\,b^2}.$$

References

1. G'Sell C, Hiver JM, Dahoun A (2002) Int J Solids Struct 39:3857
2. Galeski A (2003) Prog Polym Sci 28:1643
3. Pawlak A, Galeski A (2005) Macromol 38:9688
4. Plummer CJG, Scaramuzzino P, Kausch HH, Philippoz JM (2000) Polym Eng Sci 40:1306
5. Butler MF, Donald AM, Bras W, Mant GR, Derbyshire GE, Ryan AJ (1995) Macromol 28:6383
6. Castagnet S, Girault S, Gacougnolle JL, Dang P (2000) Polymer 41:7523
7. Zhang XC, Butler MF, Cameron RE (2000) Polymer 41:3797
8. Gacougnolle JL, Castagnet S, Werth M (2006) Eng Failure Anal 13:96
9. Cazenave J, Seguela R, Sixou B, Germain Y (2006) Polymer 47:3904
10. Alizadeh A, Richardson L, Xu J, McCartney S, Marand H, Cheung YW, Chum S (1999) Macromol 32:6221
11. Marand H, Alizadeh A, Farmer R, Desai R, Velikov V (2000) Macromol 33:3392
12. Vanderhart DL, Snyder CR (2003) Macromol 36:4813
13. O'Kane WJ, Young RJ, Ryan AJ (1995) J Macromol Sci, -Phys B34:427
14. Neidhofer M, Beaume F, Ibos L, Bernes A, Lacabanne C (2004) Polymer 45:1679
15. El Mohajir BE, Heymans N (2001) Polymer 42:5661
16. El Mohajir BE, Heymans N (2001) Polymer 42:7017
17. Nakagawa K, Ishida Y (1973) J Polym Sci Part B: Polym Phys 11:1503
18. Boyd RH (1985) Polymer 26:1123
19. Hirschinger J, Schaefer D, Spiess HW, Lovinger AJ (1991) Macromol 24:2428
20. Andre-Castagnet S, Girault S (2002) J Macromol Sci, -Phys B41:957
21. Cho K, Gent AN (1988) J Mater Sci 23:141